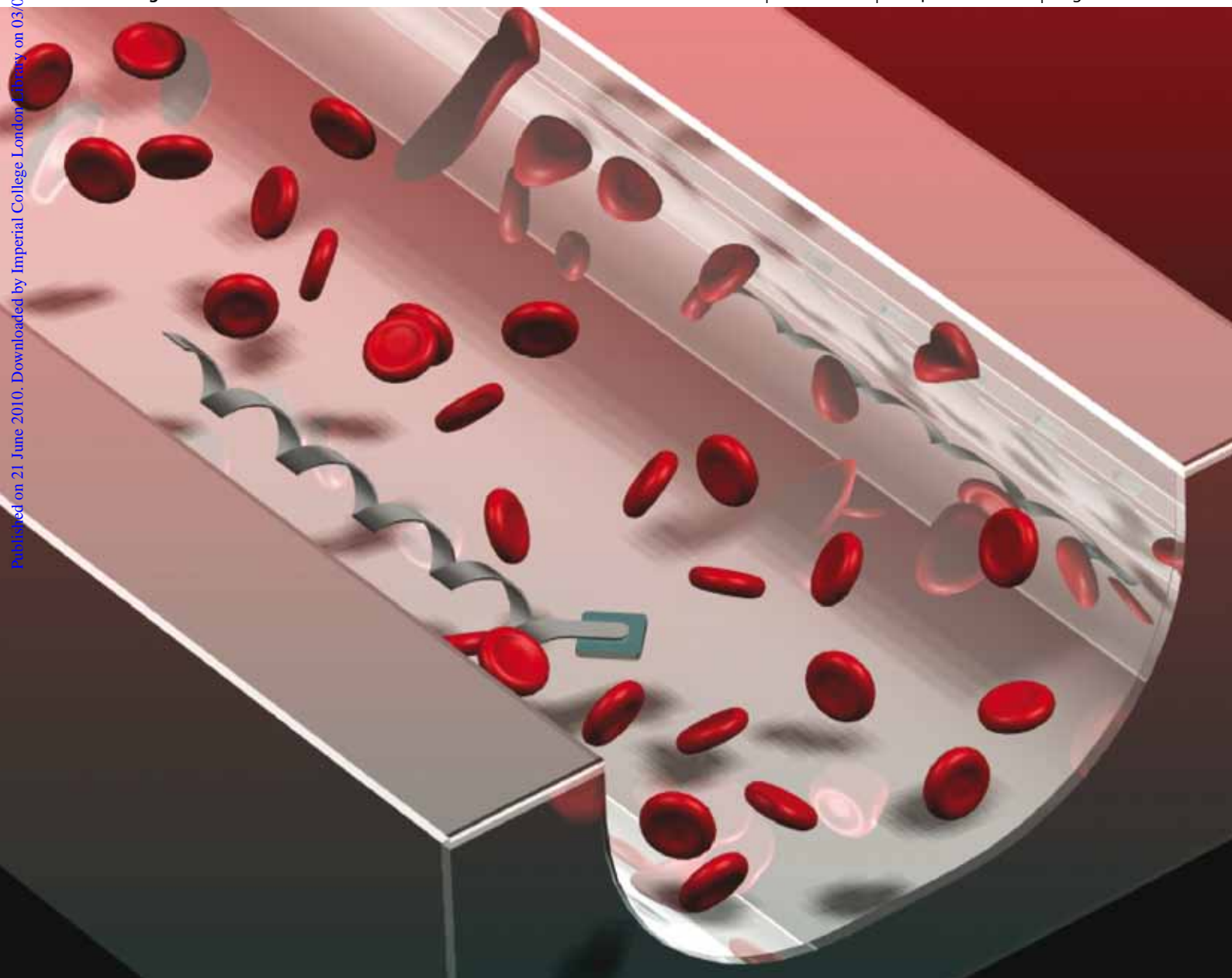


# Lab on a Chip

Micro- & nano- fluidic research for chemistry, physics, biology, & bioengineering

[www.rsc.org/loc](http://www.rsc.org/loc)

Volume 10 | Number 17 | 7 September 2010 | Pages 2177–2300



10th Anniversary: Focus on Switzerland

ISSN 1473-0197

RSC Publishing

Nelson  
Artificial bacterial flagella

Ensslin  
Quantum mechanics LOC

Frey  
Biosensor cartridge

Vogel  
Membrane nanotubes

# Artificial bacterial flagella for micromanipulation†‡

Li Zhang, Kathrin E. Peyer and Bradley J. Nelson\*

Received 17th March 2010, Accepted 2nd June 2010

DOI: 10.1039/c004450b

This article presents an overview of recent developments in artificial bacterial flagella (ABFs) and discusses challenges and opportunities in pursuing applications. These helical swimmers possess several advantageous characteristics, such as high swimming velocity and precise motion control indicating their potential for diverse applications. One application is the manipulation of small objects within liquid, which is the focus of this review. Preliminary results have shown that ABFs are capable of performing microobject manipulation either directly by mechanical contact or indirectly by generating a localized fluid flow. The latter approach can be used for batch manipulation without direct contact, also implying possibilities for flow control in lab-on-a-chip systems. Miniaturized helical swimmers are also promising for biomedical applications, such as targeted drug delivery and implantation or removal of tissues and other objects.

## 1. Introduction

In nature, microorganisms swim in a low Reynolds number regime using a variety of techniques, none of which look like macroscale swimmers.<sup>1,2</sup> The first reported investigation of swimming mechanisms at microscales dates to 1930 in which some of the locomotion strategies that small swimming organisms use were first identified.<sup>3,4</sup> Later Purcell's famous lecture and subsequent paper "Life at Low Reynolds Number"<sup>5</sup> described

how a nonreciprocating motion is required for a net displacement and his "scallop theorem"<sup>6</sup> was proposed. This concept can be demonstrated with a theoretical 3-link swimmer depicted in Fig. 1. The two hinges offer 2 degrees of freedom (DOF) and the swimmer can go through a series of angle configuration. The non-reciprocal series of configurations ABCDA (see Fig. 1a) results in a net displacement after one cycle. The series of configurations ABCBA (Fig. 1b) on the other hand is reciprocal and no net displacement is achieved after one cycle. In this highly cited paper,<sup>5</sup> he also described two techniques that microorganisms could adopt to generate nonreciprocal motion, a "flexible oar" motion and a "corkscrew" motion. The flexible oar approach is what some eukaryotes such as spermatozoa<sup>7</sup> use to propel themselves in which a propagating wave is generated by an active flagellum. A corkscrew motion is used by some prokaryotes such as *Escherichia coli* bacteria<sup>8</sup> in which a bundle of passive flagella is driven by a rotary motor into a helical shape to generate a corkscrew-like motion. A third propulsion method

*Institute of Robotics and Intelligent Systems, ETH Zurich, CH-8092 Zurich, Switzerland. E-mail: bnelson@ethz.ch*

† Published as part of a themed issue dedicated to Swiss Research: Guest Editor Professor Viola Vogel

‡ Electronic supplementary information (ESI) available: Movie S1: An ABF is steered in 3-D. The arrow at the upper left corner indicates the desired swimming direction, which is controlled by a PC. Movie S2: Manipulation of 1  $\mu\text{m}$ - and 3  $\mu\text{m}$ -diameter PS microbeads in a batch process. See DOI: 10.1039/c004450b



Li Zhang

*Li Zhang received his PhD degree from the University of Basel, Switzerland in 2007. From 2002 to 2006, he was with the Laboratory for Micro- and Nanotechnology, Paul Scherrer Institute, and also with the Department of Physics, University of Basel. In 2007, he joined the Institute of Robotics and Intelligent Systems, ETH Zurich, Zurich, Switzerland, as a postdoctoral associate, and became a senior research scientist in 2009. His current research interests include wireless sensing*

*and actuation, MEMS/NEMS devices, swimming micro-/nano-robots and their biomedical applications.*



Kathrin E. Peyer

*Kathrin E. Peyer received her BSc and MSc degree in mechanical engineering at the Swiss Federal Institute of Technology (ETH Zurich) in 2009. She joined the Institute of Robotics and Intelligent Systems lab at ETH Zurich in 2009 as a PhD student. Her fields of interest are bio-inspired robots and swimming micro-robots for biomedical applications.*

used by microorganisms such as paramecia is driven by cilia that deform in an asymmetric beat pattern.<sup>9</sup> Berg and Anderson discovered that *E. coli* swim by rotating their flagellar filaments<sup>8</sup> and that the motion is generated by a flagellar rotary motor driven by proton flow with a gradient.<sup>10</sup> A fluorescent microscopic image of an *E. coli* bacterium is shown in Fig. 1c.<sup>11</sup>

Recent developments in micro- and nanotechnology have allowed scientists to begin exploring fabricated devices capable of propulsion at the micro and nanoscale. As these micro-machines are functionalized, applications such as targeted delivery, *in vivo* sensing and manipulating cells are foreseen.<sup>12–20</sup> One of the primary challenges at these scales is power and actuation. Traditional onboard power supplies, *e.g.*, batteries, cannot be scaled to these dimensions. Thus, two main approaches have been proposed to solve this issue, using an external energy field and harvesting energy from the environment. Both approaches have been demonstrated with various artificial micro- and nano-devices swimming in their low-Reynolds number environment.<sup>4,21</sup> To date the most systematically investigated artificial swimmers are chemically driven nanomotors<sup>22–26</sup> and other chemically powered swimmers.<sup>27–31</sup> Swimmers that employ chemical locomotion<sup>32</sup> are able to harvest energy from specific chemicals in the environment, such as  $\text{H}_2\text{O}_2$ , and move independently. Several review papers have been written in recent years addressing nanomotors.<sup>32–37</sup> Two of the most interesting features of such nanodevices are their ability to manipulate microparticles<sup>24,26</sup> and their high swimming velocities of more than 100 body lengths per second.<sup>25</sup> The cheetah, as the fastest land animal,<sup>38</sup> has a speed of  $110 \text{ km h}^{-1}$ , approximately 25 body lengths per second by comparison.

An important advantage of artificial swimmers driven by external fields rather than a specific chemical environment is, of course, that they can operate within much less chemically engineered environments. The first demonstration of a wirelessly controlled helical swimmer was reported by Honda *et al.* in 1996.<sup>39</sup> It consisted of a thin helical Cu filament with a diameter of 0.15 mm and a permanent magnet at one end of the helix (Fig. 1d).

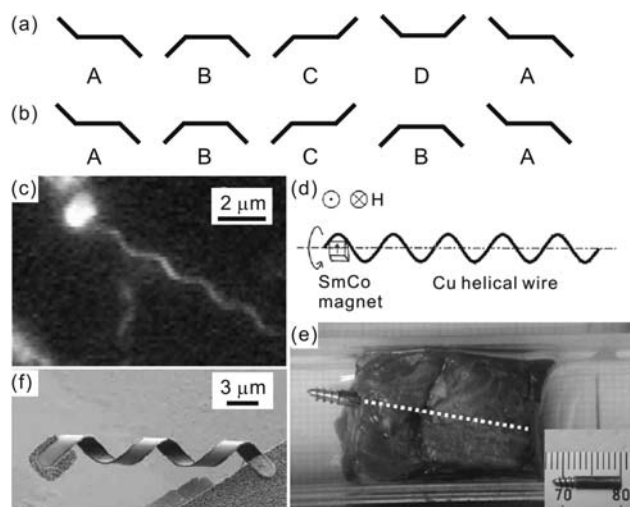


**Fig. 1** The 2-hinged theoretical swimmer proposed by Purcell: (a) the non-reciprocal series of angle configurations creates a net displacement after a whole cycle (reproduced with permission from ref. 5. Copyright 1977 American Association of Physics Teachers) and (b) the reciprocal series of configurations leads to a back and forth motion only, known as the “scallop theorem”. (c) A fluorescence microscope image of fluorescent labelled *E. coli*. *E. coli* swim by rotating helical flagella which are several micrometres long with a filament diameter of about 20 nm. Reproduced with permission from ref. 11. Copyright 2000 American Society for Microbiology. (d) Schematic of a mm long helical swimmer developed by Honda *et al.* in 1996.<sup>39</sup> The swimmer consists of a Cu helical wire and a SmCo permanent magnet “head”. The diameter of the helix and the total wire length are in the range of 0.5–1.5 mm and 5–70 mm, respectively. The cubic SmCo magnet, with each side of 1 mm, was magnetized along the direction perpendicular to the helical axis of the helical swimmer.<sup>39</sup> An alternating magnetic field ( $H$ ) is applied to rotate the helical swimmer. Reproduced with permission from ref. 39. Copyright 1996 IEEE. (e) The helical drilling micromachine rotates inside bovine meat and drills through it in 20 seconds. Inset: 10 mm long magnetic field driven microdriller developed by Ishiyama *et al.*<sup>40,41</sup> Reproduced with permission from ref. 41. Copyright 2001 Elsevier. (f) An SEM micrograph of an ABF.<sup>53</sup>



**Brad Nelson**

*Brad Nelson is the Professor of Robotics and Intelligent Systems at ETH Zürich. His primary research focus is on microrobotics and nanorobotics with an emphasis on applications in biology and medicine. He received a BSME from the University of Illinois at Urbana-Champaign and an MSME from the University of Minnesota. He has worked as an engineer at Honeywell and Motorola and served as a United States Peace Corps Volunteer in Botswana, Africa, before obtaining a PhD*

*in Robotics from Carnegie Mellon University in 1995. He was an Assistant Professor at the University of Illinois at Chicago (1995–1998) and an Associate Professor at the University of Minnesota (1998–2002). He became a Full Professor at ETH Zürich in 2002.*

The swimmer was capable of propulsion in highly viscous silicone oil, thus mimicking the locomotion technique of *E. coli*. In 2000 Ishiyama *et al.* presented a drilling micromachine based on a machined NdFeB permanent magnet with a screw-like head.<sup>40</sup> Both papers demonstrated that devices could be wirelessly steered by a rotating magnetic field. Moreover, the micromachine was able to drill through bovine meat (Fig. 1e),<sup>41</sup> heat agar gel locally,<sup>42</sup> and propel a dummy capsule endoscope in animal intestines.<sup>43,44</sup> These results demonstrated that miniaturized helical swimmers have the potential to act as untethered microsurgery tools for tasks such as removing plaque deposits in human arteries. Inspired by the motion of spermatozoa, Dreyfus *et al.* developed a microswimmer consisting of a thin paramagnetic filament that attached itself to a blood cell.<sup>45</sup> By applying an oscillating magnetic field the swimmer propelled the cell through continuous deformation of the filament in a manner somewhat similar to a eukaryotic flagellum. In 2007 our group used the self-scrolling fabrication technique<sup>46–48</sup> to fabricate helical swimmers of a size comparable to *E. coli* (see Table 1) which are capable of swimming in both water and paraffin oil.<sup>49</sup> In 2009 we demonstrated micromanipulation using a helical microswimmer, 29  $\mu\text{m}$



**Table 1** Geometrical parameters of *E. coli*<sup>11</sup> and the ABFs developed in 2007<sup>49</sup>

	Shape of swimmer	Body/"head" size/ $\mu\text{m}$	Length of helical "tail"/ $\mu\text{m}$	Diameter of helical "tail"/ $\mu\text{m}$	Thickness of helical "tail"/nm
<i>E. coli</i>	Rod-shaped body and helical shaped flagella	2.5 (Length) $\times$ 0.8 (diameter)	3–10	0.5–0.7	20
ABFs	Magnetic thin plate "head" and a helical "tail"	2 (Length) $\times$ 2 (width) $\times$ 0.2 (thickness)	30	3	27

in total length, in which colloidal microbeads with a diameter of 6  $\mu\text{m}$  were pushed and rotated.<sup>50</sup> More recently, Ghosh and Fischer presented a new technique to fabricate even smaller helical swimmers with a diameter of 200 nm and a length of 2  $\mu\text{m}$  able to push microbeads with a diameter of 5  $\mu\text{m}$ .<sup>51</sup> Helical micro/nanoswimmers have several advantages such as precise motion control and a swimming velocity similar to bacteria (*ca.* 25  $\mu\text{m s}^{-1}$ , *i.e.* 10 body lengths per second).<sup>51–53</sup>

Another approach to creating microswimmers for micro-manipulation is to harness natural bacteria as a power source. Many groups demonstrated that microobjects are able to be transported by flagellated bacteria attached on their surface.<sup>54–58</sup> The actuation force is generated by molecular motors intact in these motile bacteria. Although the motion of natural microswimmers is somewhat random compared with artificial ones, their movement can be coordinated, steered or halted by external stimuli such as light,<sup>55,57</sup> a magnetic field,<sup>56</sup> or chemicals.<sup>58</sup>

In this review we term all artificial helical swimmers that have a comparable size to bacteria (Fig. 1d) artificial bacterial flagella (ABFs). We will show recent progress in ABFs and discuss

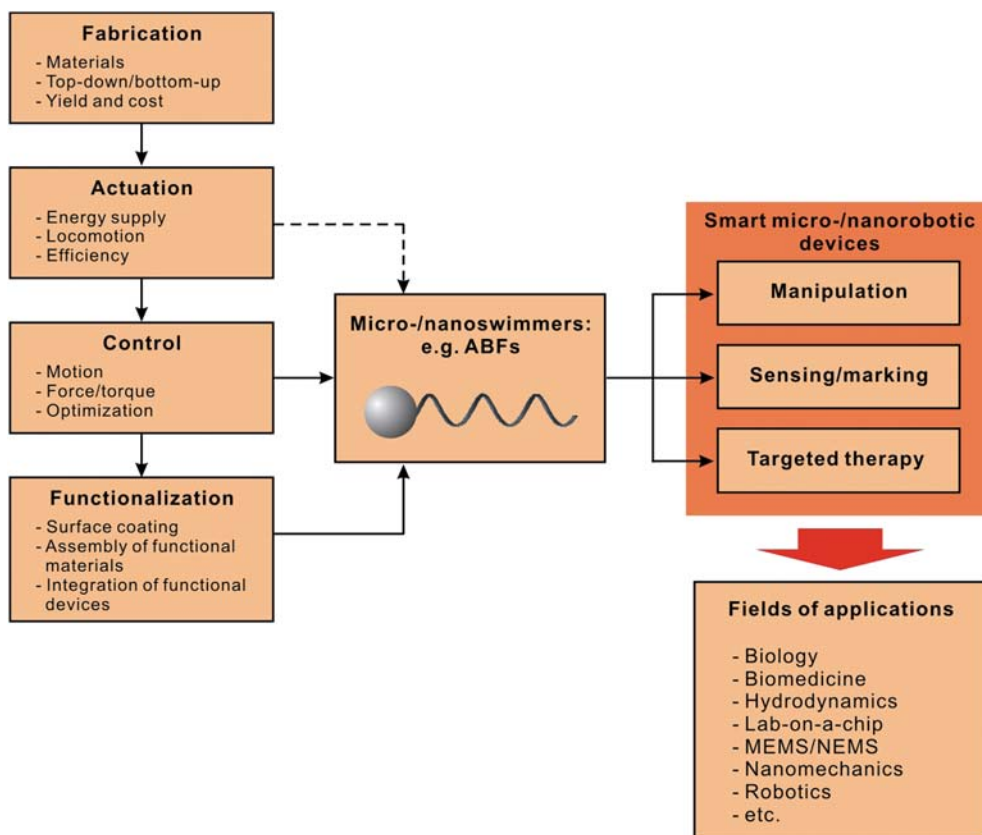
challenges and opportunities for future development. A roadmap for ABFs is shown in Fig. 2. In order to apply ABF-based micro/nanorobotic devices in diverse applications, several issues including precise motion, force and torque control, shape optimization, and functionalization must be addressed.

Points that will be addressed with regard to the development of ABFs include: motion control with an external magnetic field; separating an individual swimmer from the ensemble; force and torque control of an ABF; optimized swimming shape; and manipulation tasks that can be performed by ABFs for lab-on-a-chip applications.

## 2. Controlled fabrication and magnetic actuation

### 2.1 Fabrication

An ABF consists of a micro/nanoscale helical propeller that can be actuated to rotate along its helical axis. Unlike *E. coli*, which uses 45-nm-diameter biomolecular motors for actuation, an external magnetic field is applied to actuate ABFs, which must

**Fig. 2** A roadmap for helical swimming microrobots we call artificial bacterial flagella (ABFs).

consist at least partly of a magnetic material. The design, therefore, becomes simplified as there is no need to create a relative motion between the head and the tail of the ABF. While the fabrication of helical structures at the micro/nanometre scale is difficult for lithography-based techniques due to lithography's inherent 2-D patterning,<sup>59</sup> a number of nanohelix fabrication methods have been developed based on "bottom-up" approaches, including coiled carbon nanotubes,<sup>60</sup> semiconductive ZnO and CdS nanohelices,<sup>61,62</sup> superconducting MgB<sub>2</sub> nanohelices,<sup>63</sup> insulating Si<sub>3</sub>N<sub>4</sub> microcoils<sup>64</sup> and helical shaped polymer fibers.<sup>65</sup> Though the yield of these nanohelices is high, their geometry cannot be precisely controlled. Furthermore, fabrication is highly dependent on the material. Recently, a new technique was developed to fabricate complicated 3-D micro/nanostructures based on direct laser writing.<sup>66</sup> The shape of these as-fabricated structures is arbitrary. However, this approach is not compatible with batch processing of 3-D structures.

The fabrication of the ABFs developed in our group is based on a self-scrolling technique, which combines "top-down" lithographic patterning and a "self-organizing" step to generate 3-D structures from rolled-up planar thin films.<sup>67–70</sup> The fabrication process of the ABFs is illustrated schematically in Fig. 3a–c, and the details of the fabrication are reported elsewhere.<sup>50</sup> One main

advantage of the self-scrolling technique is that the dimension of the 3-D structures can be scaled up or down from the sub-millimetre to nanometre range in a controllable fashion.<sup>70</sup> Moreover, geometrical parameters of the helix, such as diameter, chirality, helicity angle and pitch, can be precisely controlled.<sup>46–48,71,72</sup> In addition, different materials, such as metals, dielectrics, polymers and hybrid structures, can be integrated into the structures based on thin film growth and lithographic patterning techniques.<sup>73–76</sup>

We have fabricated two different types of ABFs,<sup>50,53</sup> one with an InGaAs/GaAs semiconductor bilayer tail, and the other with an InGaAs/GaAs/Cr hybrid semiconductor–metal trilayer tail. We found that the InGaAs/GaAs/Cr helical tail is more mechanically robust than the bilayer helical tail, making the micromanipulation steps required to cut, pick and place the ABF in liquid more easily performed. The magnetic head is a square thin metal plate composed of a Cr/Ni/Au trilayer with a thickness of 10 nm/180 nm/10 nm, respectively. Fig. 3d shows an SEM micrograph of an as-fabricated ABF with an InGaAs/GaAs/Cr helical tail,<sup>53</sup> and the inset of Fig. 3d shows that the fabrication is a batch process. Assuming a 30  $\mu\text{m}$  long ABF batch fabricated on a 4 inch wafer, each one occupying a 50  $\mu\text{m}$   $\times$  50  $\mu\text{m}$  area on the surface, roughly three million ABFs can be obtained simultaneously.

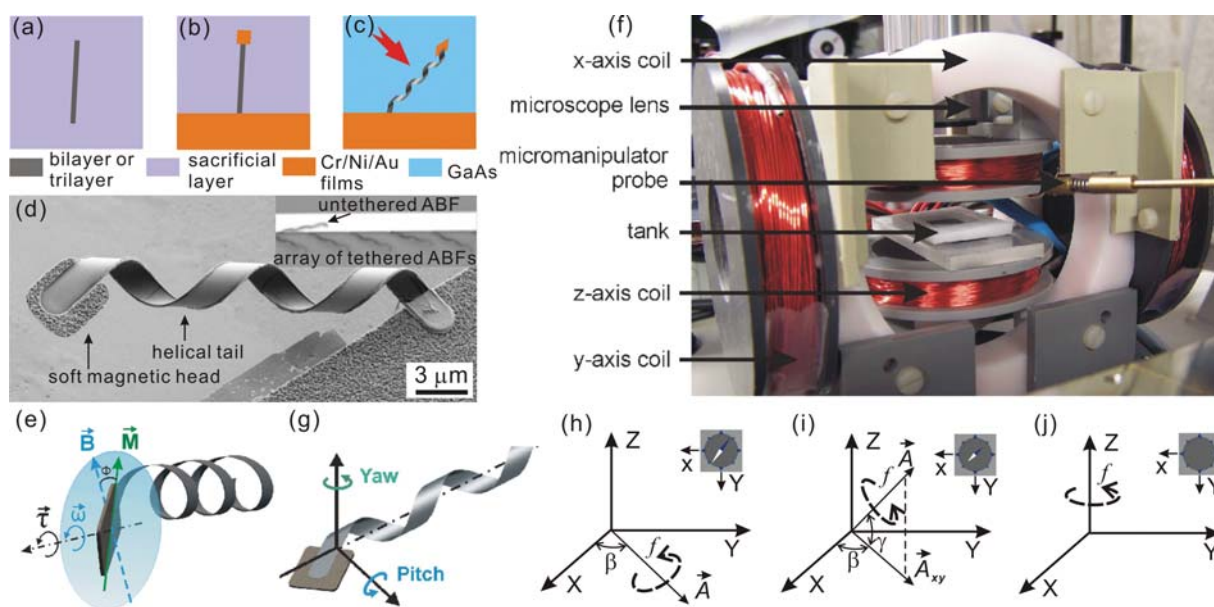


**Fig. 3** (a) After growth of the thin film, lithographic patterning processes are used to pattern InGaAs/GaAs bilayer or InGaAs/GaAs/Cr trilayer in a ribbon-like shape for the helical tail of an ABF. (b) Lift-off processes are conducted for the magnetic head of an ABF. The magnetic head is composed of a Cr/Ni/Au trilayer. (c) The ribbon-like structure self-organizes to form an ABF tethered at one end by releasing the internal stress after wet etching of the sacrificial layer. The red arrow indicates the scrolling direction of the ribbon, *i.e.*,  $\langle 100 \rangle$  on a  $(001)$  GaAs wafer. (d) FESEM micrograph of an as-fabricated ABF with a diameter of 2.8  $\mu\text{m}$ . The ABF has an InGaAs/GaAs/Cr helical tail and a thin square shaped head.<sup>53</sup> Inset: optical microscope image of a batch of tethered ABFs and an untethered ABF immersed in water. (e) Magnetic actuation. The torque ( $\tau$ ) is induced due to the misalignment between the magnetization  $\vec{M}$  of the nickel plate and the external field vector  $\vec{B}$ . The magnetic field vector  $\vec{B}$  is rotated in a plane perpendicular to the helical axis with a rotational speed  $\dot{\omega}$ . For a constant rotational speed the misalignment angle  $\phi$  between  $\vec{M}$  and  $\vec{B}$  is constant. (f) Photo of the experimental setup. The ABF swims inside the white tank which is placed in the middle of three orthogonal coil pairs. A micromanipulator is used to pick-and-place individual ABFs. A CMOS camera mounted on the optical microscope is used for recording the motion of the ABFs. (g) Yaw and pitch are the steering parameters to control the orientation of the ABF in the horizontal plane and the out-of-plane, respectively. (h) When the pitch value decreases to zero, *i.e.*,  $\gamma = 0$ , the compass needle points to the normal of the rotating magnetic field. (i) When the ABF has a pitch value between zero and 90°, *i.e.*,  $0 < \gamma < 90^\circ$ , we see the projection of the compass needle in the  $X$ – $Y$  plane, *i.e.*,  $A_{xy}$ . (j) When the pitch is equal to 90°, the compass needle disappears and the magnetic field rotates in the horizontal  $X$ – $Y$  plane. (b–d) reproduced with permission from ref. 53. Copyright 2009 American Chemical Society.

Recently, another type of artificial helical nanopropeller was reported by Ghosh and Fischer.<sup>51</sup> The helical tail of their ABF is fabricated by the glancing angle deposition (GLAD) technique,<sup>77</sup> and a permanent magnetic film is evaporated onto one side of the swimmer. The fabrication of the helical structures is a batch process with an extremely high density (*ca.* 10<sup>9</sup> per cm<sup>2</sup>), though the GLAD approach is limited to materials that can be deposited by physical vapor deposition.<sup>77</sup> This technique also requires that the magnetic film is coated on one-half of the helical nanopropeller, thus reducing the surface for functionalization by half. While the self-scrolling technique provides more flexibility for structural design, the ABFs fabricated by the GLAD process achieve an extremely high yield.

## 2.2 Magnetic actuation

An ABF is rotated along its helical axis and self-propelled somewhat similar to a corkscrew by applying a torque ( $\tau$ ). A uniform rotating magnetic field is used to actuate ABFs with which a torque is applied to the soft-magnetic metal head, as shown in Fig. 3e. The torque on a magnetized body in a magnetic field is given by:

$$\tau_{\text{m}} = \mu_0 V \vec{M} \times \vec{H} \quad (1)$$

where  $V$  and  $\vec{M}$  are the volume and magnetization of the body, respectively,  $\vec{H}$  is the applied field and  $\mu_0$  is the permeability of free space. The maximum magnetic field strength ( $|\vec{B}| = \mu_0 |\vec{H}|$ ) we apply does not generally exceed 2 mT, approximately three orders of magnitude lower than most clinical MRI systems. To actuate ABFs, the field vector  $\vec{B}$  is rotated in a plane perpendicular to the helical axis. The head of our ABFs consists of a thin square soft magnetic material made of nickel which is magnetized along its diagonal.<sup>78</sup> The magnitude of the torque grows with an increased angle between the nickel plate and the applied field. The magnetic actuation of the ABFs from Ghosh and Fischer<sup>51</sup> is based on a permanently magnetized 30 nm thick Co film, which is coated on one side of the ABF. The magnetized direction is out-of-plane of the Co film, which is perpendicular to the helical axis of the ABF. For precise steering of an ABF with a soft magnetic head, the easy axis depends strongly on its shape, which constrains the head geometry. To apply a larger torque on a helical swimmer, a magnetic material with large magnetization is desired because the volume of the magnetic material that can be incorporated is limited. One potential drawback when using a permanently magnetized material is the increased possibility of aggregation among the microswimmers, which would obviously impact swimming motion.

## 3. Motion control

### 3.1 Experimental setup

Our system uses three pairs of orthogonal electromagnetic coils to generate a uniform rotating magnetic field to actuate and control the ABFs. They are placed around the microscope lens as shown in Fig. 3f. To untether the ABFs from the chip, micromanipulation<sup>50,53</sup> and sonication<sup>51</sup> are applied. Using three orthogonally placed coil pairs the field vector and its plane of rotation can be generated with an arbitrary orientation in 3-D.

The orientation of the ABF is described with yaw and pitch values which are the orientation parameters of the ABF in and out of the horizontal plane, respectively (Fig. 3g). Thus, four parameters can be controlled independently, *i.e.*, the magnetic field strength ( $B$ ), input field frequency ( $f$ ), yaw ( $\beta$ ) and pitch ( $\gamma$ ). The translational direction is indicated as a compass needle (Fig. 3h–j). All experimental results of ABFs described in the following part of the paper were conducted in deionized water. More details of the experimental setup can be found in recent publications.<sup>50,51,53</sup>

### 3.2 Steering with micrometre precision

For forward and backward motion the ABF acts as a corkscrew to convert rotary motion to linear motion, thus forward and backward motion can be switched by simply reversing the rotating direction of the magnetic field. In contrast to reversing motion by turning the swimmer 180°, which is the method used by bacteria and other artificial microscopic swimmers, reversing rotation direction is a much more straightforward and time-efficient method, especially for use as a micromanipulation tool.<sup>50</sup>

During propulsion an ABF is steered by deviating the plane of the rotating field  $B$  such that it is no longer perpendicular to the helical axis. A steering torque is induced, and, subsequently, the ABF reorients itself to become perpendicular to the plane of the rotating field  $B$ . Isolating steering of an ABF from propulsion can also be obtained by aligning the plane of the rotating field and the helical axis in parallel.<sup>50</sup> In Fig. 4a an ABF is steered with both rotational and translational components, while in Fig. 4b the ABF is simply rotated. Movie S1 (available in the ESI†) shows an ABF is steered by a rotating magnetic field. Fig. 4c shows an ABF swimming towards a target of diameter 10  $\mu\text{m}$ . The time to align with the steering input increases as the swimming speed of the ABF grows, which implies a tradeoff between torque available for propulsion and torque available for steering. Torque for propulsion reaches a maximum as the misalignment angle  $\phi$  reaches 90° (Fig. 3e), whereas the torque for steering is reduced to zero. It is, therefore, less efficient to steer and propel the ABF simultaneously. A better way to swim towards a target is to orient the ABF and, subsequently, use the torque for propulsion only. The resulting swimming style consists of an alternating fast, straight motion with a sudden change in direction. Interestingly, this is the same manner with which bacteria swim in nature, *i.e.*, by switching between propulsion and tumbling. An important difference between bacteria and ABFs is that, although they both swim in the same Reynolds number regime, bacteria have a density similar to water, while ABF must overcome its weight and swim at least partially upwards.<sup>53</sup>

### 3.3 Velocity control

The dependence of the velocity ( $v$ ) of a 38  $\mu\text{m}$  long ABF on the rotation frequency ( $f$ ) is characterized in Fig. 4d.<sup>53</sup> Three different field strengths, 1.0 mT, 1.5 mT and 2.0 mT, were applied for the tests. The field's rotational frequency was increased from 5 Hz to 35 Hz. The curves show that a maximum velocity exists; if the frequency increases further, velocity reduces because the available magnetic torque is no longer sufficient to keep the ABF



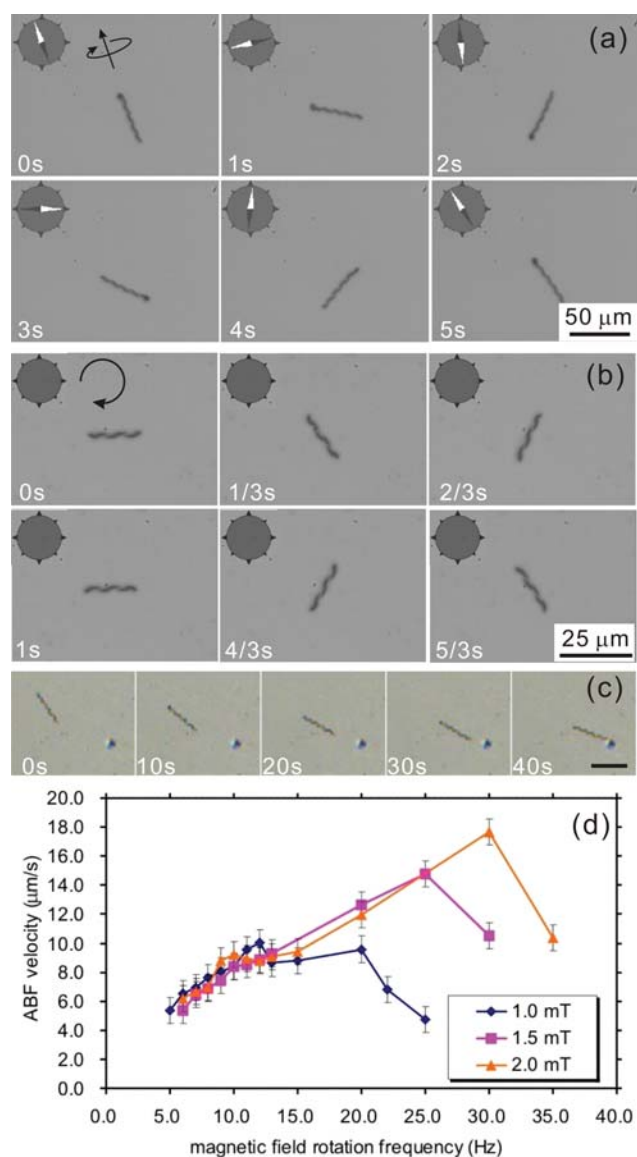


**Fig. 4** Steering an ABF. (a) Optical microscope images of the turning motion of an ABF controlled by magnetic fields in the horizontal  $X$ - $Y$  plane. The ABF completes 1 turn in *ca.* 5 s. The commanded translation and rotation directions of the ABF are indicated by the arrows. (b) Pure rotational motion of the ABF with frequency of 0.5 Hz. The ABF rotates in sync with the field. The arrow indicates the rotational direction of the ABF. (c) ABF swims towards a target (dark dot) and reaches it after 40 seconds.<sup>50</sup> The scale bar is 40  $\mu\text{m}$ . Reproduced with permission from ref. 50. Copyright 2009 American Institute of Physics. (d) Dependence of ABF velocity on strength and rotation frequency of the applied magnetic field. Data were experimentally collected for a 38  $\mu\text{m}$  long ABF swimming mostly horizontally. The error bars are attributed to the uncertainty in the position of the ABF based on the resolution of the recorded images. Reproduced with permission from ref. 53. Copyright 2009 American Chemical Society.

synchronized with the applied field. This behavior is consistent with low-Reynolds-number experiments with macroscale helical swimmers.<sup>39–41,79</sup> This maximum synchronized frequency is referred to as the step-out frequency ( $f_{\text{step-out}}$ ). The maximum velocity we achieved with a 2 mT field is approximately 18  $\mu\text{m s}^{-1}$ .<sup>53</sup> The results also indicate that by exerting a stronger

magnetic torque on the ABF higher driving frequencies can be achieved resulting in higher linear velocity, and that the maximum velocity is linearly proportional to the strength of the applied field. The results also show that the swimmer's rotation is synchronized with the applied field while the frequency is less than  $f_{\text{step-out}}$ , and that the ABF velocity decreases linearly with frequency, as expected in the low-Reynolds-number regime.<sup>5</sup> The ABFs of Ghosh and Fischer showed a linear frequency–velocity relationship as well, and their swimmer achieved a maximum velocity of 40  $\mu\text{m s}^{-1}$ , which is equivalent to 20 body-lengths per second.<sup>51</sup> The swimming tests of ABFs were always conducted in deionized water with a viscosity of 1 mPa s at room temperature. For the swimming tests of *E. coli*, Berg *et al.* used a motility buffer with a viscosity of 0.93 mPa s and found that the average swimming speed of a sample with 73 *E. coli* cells is  $25 \pm 8 \mu\text{m s}^{-1}$  (*i.e.*  $10 \pm 3.2$  body lengths per second) at room temperature.<sup>80</sup> Unlike the ABFs driven by the external magnetic field, the motility of bacteria is strongly influenced by the chemicals and temperature of the environment.

### 3.4 Drifting and wobbling

It is known that some bacteria tend to swim in circles near solid boundaries due to the counter-rotation of the bacterium body and its flagellum, each tending to roll along the wall in opposite directions resulting in a net torque on the microorganism.<sup>81</sup> Solid boundaries also affect the swimming of ABFs.

The rotating bodies of ABFs tend to roll along solid surfaces, even when there is no direct contact due to an increase in viscous drag near a wall. Unlike bacteria the ABF has no tendency to swim in circles because the helical tail rotates passively with the magnetic head. The symmetry of the drag acting along the length of the ABF is broken if one end is further away from the wall than the other. This is the case in Fig. 5 where an ABF crosses over an edge and rotates. Previous results also showed that the drift from the wall effect is negligible when the ABF swims vertically.<sup>53</sup>

The swimming behavior of an ABF in a low-frequency range was also investigated and a precession phenomenon was

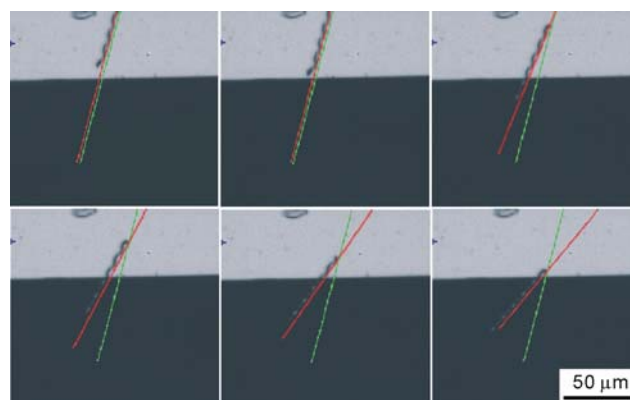


**Fig. 5** ABF swims over an edge. Due to different drift effects at the two ends of the ABF a torque is generated to rotate the ABF clockwise toward the edge of the solid surface and the free surface. The Si wafer surface has higher brightness due to the stronger light reflection, and the free space is the dark area.

observed at frequencies less than *ca.* 5 Hz.<sup>82</sup> The experimental results show that, although the ABF rotated in sync with the input field, it wobbled about its helical axis with a constant precession angle. The wobbling angle increases significantly at input frequencies below 2 Hz which leads to a larger sideward than forward velocity.<sup>82</sup> For precise steering these wall effects must be taken into account as they influence the propulsion direction of the swimmer.

While motion artifacts such as drift lead to less homogenous motion, it is possible that these effects can be utilized for separating an ABF from a swarm, *i.e.*, by designing a variety of ABF prototypes that exhibit a difference in drift behavior which can be used as a sorting mechanism.

### 3.5 Force and torque control

Because ABFs swim in a low Reynolds number regime Stoke's flow predominates, and a propulsion matrix linearly relates the force ( $F$ ) and torque ( $\tau$ ) of a helical swimmer with its velocity ( $v$ ) and angular speed ( $\omega$ ) in which<sup>5,83</sup>

$$\begin{bmatrix} F \\ \tau \end{bmatrix} = \begin{bmatrix} a & b \\ b & c \end{bmatrix} \begin{bmatrix} v \\ \omega \end{bmatrix} \quad (2)$$

In one approach optical tweezers were used to trap *E. coli* and estimate its propulsive force. From this the propulsion matrix can be determined.<sup>84</sup> For our ABF the parameters of the matrix were estimated by a series of experiments.<sup>53</sup> Eqn (2) was used to determine the maximum pushing force and torque. For example, the three coefficients for a 38  $\mu\text{m}$  long ABF are calculated as  $a = 1.5 \times 10^{-7} \text{ N s m}^{-1}$ ,  $b = -1.6 \times 10^{-14} \text{ N s}$ ,  $c = 2.3 \times 10^{-19} \text{ N m s}$ . It was shown that with a 2 mT field a maximum force  $F_{\text{max}} = 3.0 \text{ pN}$  is sufficient to move a microscale object such as a blood cell. The maximum torque is  $\tau_{\text{max}} = 43 \text{ nN nm}$ , which is *ca.* two orders of magnitude larger than that of the molecular motor in *E. coli*.<sup>10,84</sup> Unlike chemically driven artificial nanomotors or bacterial molecular motors, the magnetic torque and propulsive force of the ABFs can be controlled smoothly over a large linear range of the  $v$ - $\omega$  plot simply by tuning the frequency of the input field.

## 4. Shape optimization

The optimization of the shape of a helical artificial swimmer is important for improving swimming performance independent of the input field. Ghosh and Fischer reported that their ABFs swim with a high efficiency by advancing almost one pitch translation per rotation.<sup>51</sup> By reducing the diameter of the ABFs from 2.8  $\mu\text{m}$  to 0.8  $\mu\text{m}$  and the length from 30  $\mu\text{m}$  to 8  $\mu\text{m}$ , we observed that the relative swimming velocity increases with the same input

frequency. Table 2 compares our results with data from Ghosh and Fischer.<sup>51</sup> The results indicate that the ratio ( $v/L$ ) of the translational displacement per rotation becomes higher as the dimension of the helical swimmer decreases, hence, the ABFs are propelled more efficiently.

The effects of head size and tail length on swimming velocity were investigated in two experiments. For a comparison of the swimming velocity of ABFs with different head sizes, two 4.5-turn ABFs were tested (head dimensions 4.5  $\mu\text{m} \times 4.5 \mu\text{m} \times 200 \text{ nm}$  and 2.5  $\mu\text{m} \times 2.5 \mu\text{m} \times 200 \text{ nm}$ ).<sup>53</sup> The results are depicted in Fig. 6a and show that an ABF with a large head swims slower due to the larger fluidic drag when the input frequency is lower than the  $f_{\text{step-out}}$ . However, the ABF with the large head has a larger maximum swimming velocity because a larger magnetic torque can be applied to reach a higher  $f_{\text{step-out}}$ . For a given tail a trade-off exists between increasing the magnetic torque and decreasing the induced fluidic drag to gain the maximum velocity. The results also show that different head sizes can be used to decouple individual ABFs from a swarm. It has been shown experimentally that by tuning the input frequencies, an ABF with a small head can be immobilized inside a micro-fabricated channel, while others with large heads keep swimming.<sup>85</sup> In another experiment, ABFs with the same geometrical parameters except for the tail length were also tested, and results show that the  $f_{\text{step-out}}$  of the ABFs with a longer tail is lower, whereas the velocity difference is not evident when the frequency is lower than the  $f_{\text{step-out}}$ .

A simplified model (Fig. 6b) was used for the hydrodynamics simulations to determine the influence of ABF shape parameters on swimming. In the model, a helical swimmer consists of a spherical head with a diameter of  $d$  and a helical tail filament with a diameter of  $2\sigma$ . First, we consider the helical tail which is responsible for the net forward propulsion of the helical swimmer. On an infinitesimally small cylindrical element of the filament, the force equilibrium can be found between the driving force and the drag force acting on the element. The net forward propulsion is created due to the difference in drag resistance of the perpendicular flow and the flow along the cylindrical element axis. We then consider the head of the helical swimmer which simply induces a resistive drag force and torque that varies linearly with the forward velocity and rotational speed, respectively. The maximum velocity ( $v_{\text{max}}$ ) is limited by the maximum magnetic torque ( $\tau_{\text{max}}$ ) and can be written as:<sup>53</sup>

$$v_{\text{max}} = \frac{b}{b^2 - ac} \tau_{\text{max}} \quad (3)$$

in which  $a$ ,  $b$  and  $c$  are parameters in the propulsion matrix (eqn (2)). In order to see whether an optimized head size exists,  $v_{\text{max}} = f(d/\sigma)$  was simulated for different values of  $n$  and the results are depicted in Fig. 6c.<sup>53</sup> Simulation results indicate that an optimal head size for a given helical tail becomes a matter of finding the optimal trade-off between maximizing the magnetic torque input and minimizing the drag.<sup>53</sup> The simulation plots also indicate that the maximum velocity of the ABF is larger with a longer tail, however, this is not the case in our previous experiment. The reason is mainly attributed to unmodeled gravity and intermolecular interactions of the ABF with the substrate.

The helical tail of the ABF is the other important structure that must be considered for optimization. Several classical

**Table 2** Dependence of the dimensions of the helical swimmers to the conversion ratio of the translational movement to rotational movement

Swimming at 10 Hz	Number of turns ( $n$ )	Total length $L/\mu\text{m}$	Diameter $d/\mu\text{m}$	Velocity $v/\mu\text{m s}^{-1}$	Relative velocity ( $v/L$ )	Ratio ( $v/Lf$ )
ABF <sub>1</sub>	3.5	30	2.8	6	0.2	0.02
ABF <sub>2</sub>	3.5	8	0.8	4	0.5	0.05
ABF <sub>3</sub> <sup>51</sup>	4	2	0.2	2	1	0.1



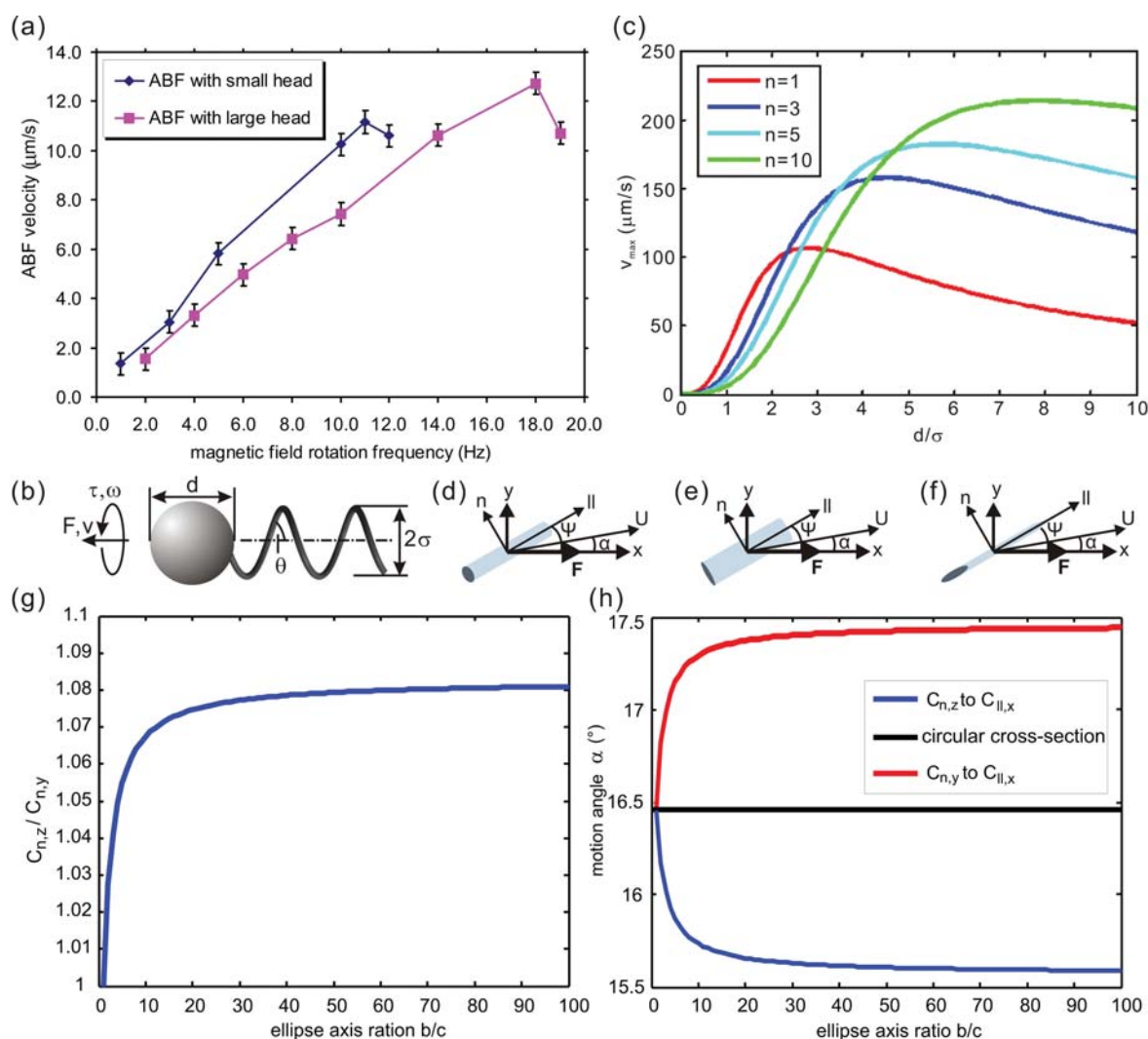


**Fig. 6** (a) Dependence of ABF velocity on the size of the head. The ABF with a larger head has a smaller velocity slope than the ABF with a smaller head. Both of the ABFs have 4.5 turns and the strength of the magnetic field is 2 mT. Reproduced with permission from ref. 53. Copyright 2009 American Chemical Society. (b) Model of the helical swimmer. The parameters are shown in the schematic.  $F$  and  $\tau$  are defined as the propulsive force and the applied torque;  $v$  and  $\omega$  are the translational and the rotational velocity;  $d$  and  $2\sigma$  are the diameter of the sphere and the helical filament;  $\lambda$  and  $\theta$  are the pitch and the complement angle of helicity angle of the helical filament. (c) The dependence of  $v_{\text{max}}$  on the head size for the four ABFs with different tail lengths in turns  $n$ . The diameter of the swimmer heads is normalized by the major helix radius  $d/\sigma$ . (d–f) A cylinder is pulled with a force  $F$ . The cylinder has either a circular cross-section (d) or an elliptical cross-section. Either the thin (e) or the broad (f) side of the ellipse faces the pulling direction. (g) Drag ratio  $C_{n,z}/C_{n,y}$  of a cylinder with elliptical cross-section. The drag perpendicular to the long ellipse axis  $C_{n,z}$  is larger than  $C_{n,y}$ . (h) The horizontal black line is the drag ratio  $C_n/C_{\parallel}$  of a cylinder with circular cross-section. Also,  $C_{\parallel}$  remains constant and the changes in the ratio  $C_n/C_{\parallel}$  are due to the variation of the perpendicular component  $C_n$ .

theories have been developed to explain the propulsion of flagellated bacteria, such as Taylor's swimming sheet, local drag theory, and slender-body theory.<sup>4,86–90</sup> In our simulation, a simple 2-D model and local drag theory was adopted. An infinitesimal segment of the helical filament is shown in Fig. 6d in which it is assumed that the cylinder is pulled with a force in the  $x$ -direction. The cylinder has an angle of  $\psi$  with respect to the  $x$ -axis, and  $U$  is the resulting direction of the motion. By applying a force in the  $x$ -direction a velocity component perpendicular to the direction of actuation is generated. Obviously, this is the principle that transforms the torque input of the helix into a translational motion. It is desirable to maximize the angle  $\alpha$  and, hence, to induce the maximum velocity component in the

$y$ -axis. This corresponds to a maximum forward velocity of the helix for a given torque input. The result of this simplified model predicts an optimal helicity angle ( $\theta$ ) of between 50 and 60 degrees,<sup>91</sup> consistent with previous reports.<sup>92,93</sup> Other simulations based on slender-body theory show that the optimal angle is 45° for both 2-D (planar wave) and 3-D (helical filament) simulations.<sup>4,94,95</sup> The as-fabricated ABFs have a helicity angle of approximately 45° which can be tuned to a larger or smaller value.<sup>50,53</sup>

Compared with other published models, this simplified model provides us with analytical, and therefore more intuitive, equations showing the influence of the drag imbalance on the helical filament propulsion. In particular it allows the incorporation of

non-circular tail filaments in a straightforward way. This is interesting as our current ABF design does not have a circular cross-section. For the simulations a cylinder with an elliptical cross-section is used. We assume that the cylinder can be arranged either with the thin or the broad side facing the direction of motion as shown in Fig. 6e and f, respectively. The drag along the axis of the cylinder ( $C_{\parallel}$ ) is the same in both cases, but the drag coefficients perpendicular to the cylindrical axis ( $C_{\perp}$ ) are different. Fig. 6g shows the ratio of the drag coefficients  $C_{\perp,z}/C_{\perp,y}$  over different ellipse axis ratios in which the ratio  $C_{\perp,z}/C_{\perp,y}$  is equal to one for a circular cross-section and increases for larger ellipse axis ratios. The simulation shows that the ratio  $C_{\perp,z}/C_{\perp,y}$  increases by less than 9% from a circular cross-section to a ribbon, even with an aspect ratio of 100, which implies that this shape effect is not crucial. According to the local drag theory, the angle  $\alpha$  can be expressed as:<sup>91</sup>

$$\alpha = \tan^{-1} \left( \frac{\sin \psi \cos \psi (C_{\perp} - C_{\parallel})}{C_{\parallel} \sin^2 \psi + C_{\perp} \cos^2 \psi} \right) \quad (4)$$

The influence of the elliptical shape on the motion angle  $\alpha$  is shown in Fig. 6h, in which the black line shows the ratio  $C_{\perp}/C_{\parallel}$  for a circular cross-section, while the red line indicates that the ratio increases for the cylinder with the broad side of the ellipse facing the direction of motion (Fig. 6e). Fujita and Kawai, applied a boundary integral method to model a flagellated microorganism, also reported that an optimal helical filament should have a non-circular cross-section with the broad side facing the direction of the applied force.<sup>96</sup> This result indicates

that our current ABF prototypes use a non-ideal helical tail, because the thin side of the ribbon is facing the direction of the applied force. Due to the self-scrolling fabrication method it is difficult, however, to adjust the helical tail design in that respect. Nevertheless, even if an ideal helix with an optimal ellipse cross-section could be realized, the increase in  $\alpha$  is rather small.

## 5. Manipulation and integration

Self-propelled devices such as ABFs can provide a versatile tool for manipulating cellular or sub-cellular objects. In principle, two different manipulation methods could be applied: (i) contact manipulation, in which ABFs contact the microobjects and manipulate them directly and (ii) non-contact manipulation, in which ABFs manipulate the microobjects by generating a controlled fluid flow.

Typical contact manipulation tasks that ABFs have the potential to perform are shown in Fig. 7a–f.<sup>97</sup> A swimming ABF could perform pushing (Fig. 7a), twisting (Fig. 7b), rotating (Fig. 7c), injecting (Fig. 7d), applying pressure at a defined position of a cell (Fig. 7e), and, drilling, sensing and delivering drug into a cell (Fig. 7f). Contact manipulation, such as pushing and rotating, was discussed earlier.<sup>50,51</sup> In general, an unfixed point contact between the ABF and the microobject is not the best solution for cargo transport, therefore, other approaches should be considered for stable loading and unloading. Recently, Wang *et al.* showed that a magnetic microbead could be picked-and-placed by a Au/Ni/Au/Pt-CNT nanomotor in a microchannel, where the loading and releasing are based on the control of the magnetic attractive force.<sup>24</sup> Self-assembly of the nanomotors and the polystyrene cargo have also been achieved by electrostatic force or chemical interaction on one end of the nanomotor and surface functionalized microbeads.<sup>26</sup> Dreyfus *et al.* assembled a blood cell on a paramagnetic filament and applied an oscillating magnetic field to transport it.<sup>45</sup> Thus, self-assembly is a promising method to load the microobject on the swimmer with a sufficiently large bonding force. However, releasing the microobject requires other means, *e.g.* chemical, since intermolecular forces or stronger chemical bonding must be overcome. Alternatively, to perform cargo transport in a stable and repeatable fashion, a multi-point contact condition between the swimmer and the microobject is one solution. A previously proposed wirelessly controlled robotic microhand could be a good candidate for that purpose,<sup>98–100</sup> since it is able to pick-and-place cells. Though the robotic microhand is actuated with a magnetic field, it is displaced with a relatively low precision control. Previously, Gracias' group demonstrated other tetherless 3-D tools such as a micro-container capable of self-loading cells and drug delivery (Fig. 8).<sup>101</sup> Such tetherless 3-D devices could be integrated in rolled-up ABFs to enhance the functionality of the artificial swimmer, since they are all fabricated using a similar self-scrolling technique.<sup>70</sup> For a manipulation task, such as applying pressure on a defined position of a cell membrane for bio-microrheology study,<sup>102</sup> the small cross-sectional area of the ABFs has the advantage of applying a large pressure (approximately a few newtons per square metre<sup>51</sup>). However, for cell membrane penetration, this pressure might be not sufficient. Sanchez *et al.* applied

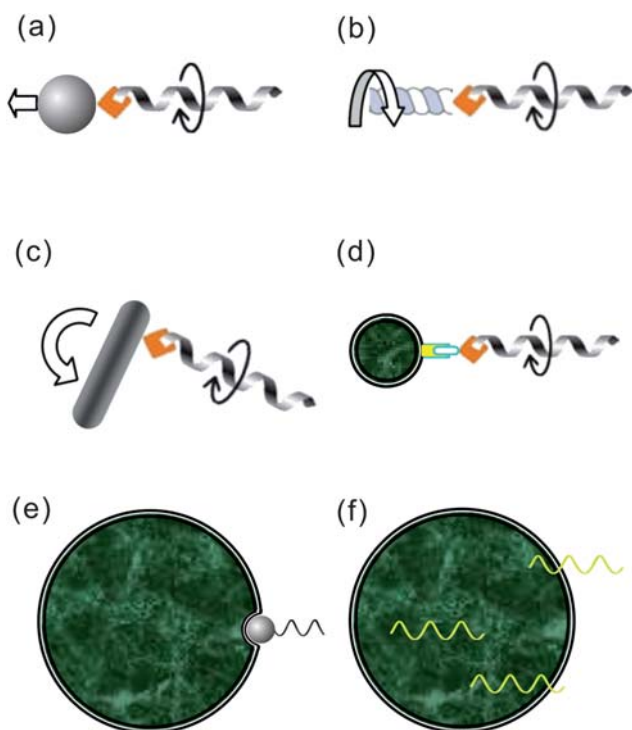


**Fig. 7** Conceptual sketch of contact manipulations using an ABF: (a) pushing/transport, (b) twisting, (c) rotating, (d) injecting, (e) characterizing local mechanical properties of cells (bio-microrheology), and (f) penetrating/sensing/delivering drug. (a–d) reproduced with permission from ref. 97. Copyright 2009 IEEE.

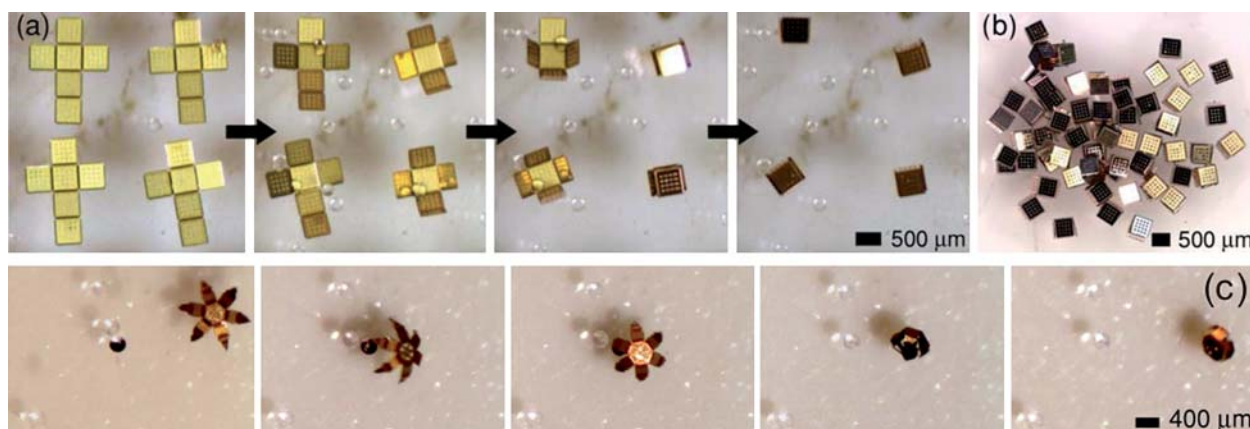


**Fig. 8** (a and b) Self-loading of 500 μm micro-containers with 250 μm microbeads. The microcontainers could be fabricated to deliver cells or drugs. Reproduced with permission from ref. 101. Copyright 2008 Royal Society of Chemistry. (c) Optical microscopy sequence showing the remote-controlled, thermally triggered capture of a dyed bead (275 μm) from several clear beads. Reproduced with permission from ref. 100. Copyright 2009 National Academy of Sciences, U.S.A.

hydrostatic pressure through a pipette to measure the local mechanical properties of living cells.<sup>103</sup> It was found that the fixed epithelial cell membrane is penetrated at a pressure of about 100 kPa with a pipette velocity of about  $0.1 \mu\text{m s}^{-1}$ . Recently, many groups have performed cell membrane penetration using nanoneedles.<sup>104</sup> It was reported that, for human epidermal melanocytes, nanoneedles of 200–300 nm in diameter required penetration forces of 0.5–2.0 nN,<sup>105,106</sup> which would be difficult to generate with the current ABF designs.<sup>50,51</sup> In fact, cell membrane penetration also depends on many other factors,<sup>103,104</sup> such as the types of cells, the injection speed and approaching angle of the injection tool, and the chemical properties at the interface of the injection tool and the cell membranes. Cai *et al.* achieved the mammalian cell penetration and DNA delivery using carbon nanotubes (CNTs) with a diameter of *ca.* 50 nm encapsulated with elongated magnetic particles at their tips. A magnetic field was applied to drive the CNTs towards the cells for the injection.<sup>107</sup> Kim *et al.* showed that mammalian cells such as mouse embryonic stem (mES) cells and human embryonic kidney (HEK 293T) cells could be penetrated by Si nanowires (NWs) of 1–100 nm in diameter without applying any external force.<sup>108</sup> This indicates that cell membrane penetration could be realized by ABFs as the cross-sectional area of the ABFs becomes sufficiently small. Therefore magnetic field driven helical shaped NWs or NTs (NWs/NTs based ABFs) should be good candidates for cell injection and targeted drug delivery. It is notable that CNT nanocoils encapsulated with magnetic particles were realized more than a decade ago.<sup>60</sup> However, for controlled swimming and cell membrane penetration, the fabrication of nanocoils and the magnetic segment must be developed and optimized, *e.g.* the length of the nanocoils, the shape, size and orientation of the magnetic segment.

In contrast to direct manipulation, fluid flow manipulation of microobjects by a swimmer opens a new path for transporting microobjects in a batch process. Polystyrene (PS) tracer micro-particles (Polysciences, Inc.) with a diameter of 1 μm were employed for manipulation tests. Fluid flow generated by a swimming ABF near a solid boundary can be monitored by

these tracers. Results show that when the tracers are close to the sides of the ABF, they are transported in approximately the same translational direction, *i.e.*, downwards in the image, as shown in Fig. 9a. When the distance of the tracer beads from the ABF increases, *i.e.*, when the fluid flow generated by the swimming ABF is negligible, the tracers “a”, “b” and “c” exhibit Brownian motion (after approximately 4 seconds, 6 seconds and 8 seconds, respectively). Additionally, the velocity of the tracers is increased as they move closer to the ABF, reaching a maximum when they are pulled across the ABF from one side to the other. Due to the larger fluidic drag near the solid surface, the fluid flow surrounding the horizontal ABF is highly asymmetrical which leads to the unidirectional transport of the tracers. An ABF, therefore, could act as a local fluidic pump to move microobjects towards a specified direction near a wall. The tracking lines of three tracers are shown in Fig. 9. Non-contact manipulation tests were also conducted in a microchannel shown in Fig. 9b. A swimming ABF is capable of pumping nearly all randomly distributed 3 μm diameter PS microbeads (Polysciences, Inc.) to one side of the microchannel when it swims from one end to the other end of the channel. Movie S2 (available in the ESI†) shows fluid flow manipulations of microobjects. The ABF could be locked in place with a magnetic gradient force counterbalancing the fluid propulsion force<sup>109</sup> in which the ABF acts as a stationary pump. Turning off the gradient force would allow the ABF to swim and hence the pump’s location moved. Further experimental results also showed that the tracers rotate around the ABF when it is vertical to a surface, and their velocity decreases as distance to the ABF increases.

The results imply that, for fluid flow manipulation, a swimming ABF can serve as a local pump (Fig. 9c), sorter (Fig. 9d) and mixer (Fig. 9e) of microobjects. Moreover, ABFs provide mobile manipulation tools for local flow control,<sup>110</sup> such as pumping (Fig. 9f) and mixing (Fig. 9e). For micromanipulation, magnetic approaches have the advantage that they do not require high-intensity lasers<sup>111</sup> or a special environment of a particular chemical composition that serves as a fuel<sup>34</sup> making miniaturized helical swimmers interesting candidates for lab-on-a-chip applications.



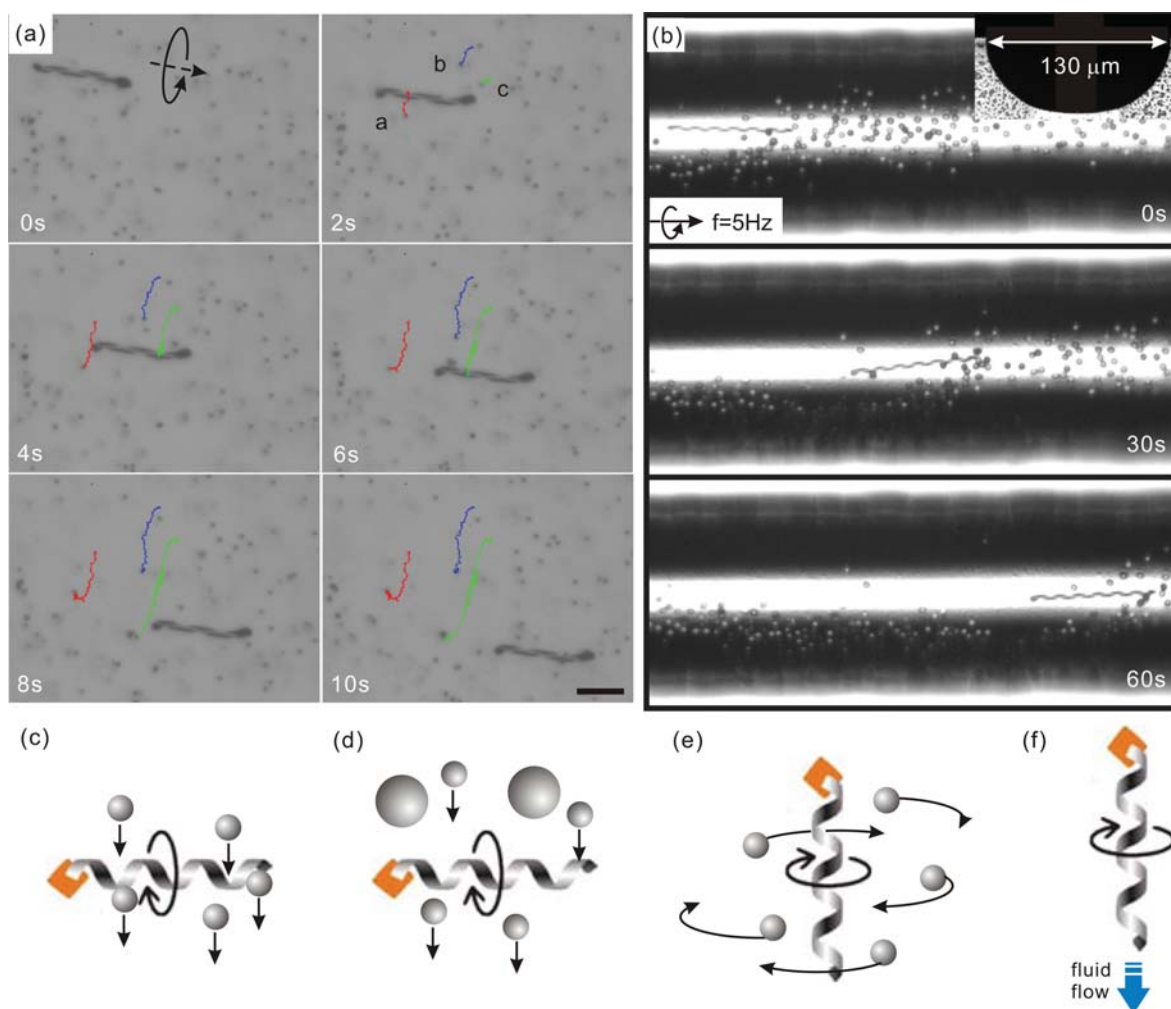


**Fig. 9** (a) The tracking lines of the three tracer particles show the fluid flow generated by the horizontal ABF. The ABF swims at a frequency of 10 Hz with 2 mT field strength. The fluid flow generated by the ABF transports the tracers from one side of the ABF to the other side (downward in the image). The arrows show the commanded rotational and translational directions of the ABF. (b) An ABF swims inside a 130  $\mu\text{m}$  broad microchannel in which 3  $\mu\text{m}$  diameter microbeads are randomly distributed. Almost all beads are pumped to one side of the ABF (downward in image) after the ABF swims through them. Input frequency is 5 Hz and the field strength is 2 mT. Inset: optical microscope image shows the cross-section of the microchannel. Conceptual sketch of non-contact manipulations using an ABF: (c) translating microobjects/pumping fluid near a surface (top-view), (d) sorting microobjects near a surface (top-view), (e) rotating microobjects/mixing fluid (side-view) and (f) pumping fluid flow backward as a stationary pump.

## 6. Conclusions and future outlook

Recent developments in ABFs show that these self-propelled helical microswimmers can be steered in 3-D by a low-strength, rotating magnetic field with micrometre positioning precision. Moreover, the force and torque can be estimated and tuned over a large range by changing the input field once the propulsion matrix is experimentally determined. Unlike other micro-swimmers previously demonstrated that manipulate individual microobject by direct contact, we demonstrate that self-propelled devices are also able to manipulate microobjects in parallel based on localized fluid flow control. Furthermore, ABFs are capable of performing fluidic manipulation as stationary pumps and mixers, making helical swimming microrobots candidates for wirelessly controlled components of lab-on-a-chip devices. These magnetically driven helical devices also have the potential to act as wireless manipulators for medical and biological applications

under 3-D control in fluid environments. Once functionalized, ABFs have the potential to sense and transmit inter- or intra-cellular information, and to perform targeted delivery of energy (e.g. inductive heating) and of chemical and biological substances. One challenge here is to design miniaturized helical swimmers with large force and torque output. For *in vivo* applications, another challenge involves fabricating ABFs with biocompatible materials. Previously, an approach was reported to fabricate mm size PDMS swimmers embedded with ferromagnetic nanoparticles actuated by a rotating magnetic field.<sup>112</sup> Furthermore, by replacing the ferromagnetic nanoparticles with coated ferromagnetic nanoparticles, their functionality, biocompatibility<sup>113</sup> and even tracking signal can be improved for *in vivo* applications.<sup>114</sup> Unlike the magnetic control of ABFs developed before<sup>50,51</sup> magnetized nanoparticles distributed in the polymer body will be actuated and navigated using a magnetic field which could be tricky. Additionally, to apply the

microrobots *in vivo*, steering and monitoring of these helical swimmers in a dynamic liquid, will be challenging, especially in a viscous non-Newtonian fluid.

## Acknowledgements

The authors thank the FIRST lab at ETH Zurich for technical support of micro-fabrication. The authors are also grateful to Prof. Lixin Dong (Michigan State University, USA), Prof. Jake J. Abbott (University of Utah, USA) and Dr Peer Fischer (Fraunhofer Institute, Germany) for their fruitful discussion, and Dr Bradley E. Kratochvil (ETH Zurich, Switzerland) for providing technical support of the experimental setup. Funding for this research was partially provided by the Swiss National Science Foundation (SNSF).

## References

- 1 S. Childress, *Mechanics of Swimming and Flying*, Cambridge University Press, Cambridge, 1981.
- 2 S. Vogel, *Life in Moving Fluids*, Princeton University Press, Princeton, NJ, 1996.
- 3 W. Ludwig, *J. Comp. Physiol., A*, 1930, **13**, 397–504.
- 4 E. Lauga and T. R. Powers, *Rep. Prog. Phys.*, 2009, **72**, 096601.
- 5 E. M. Purcell, *Am. J. Phys.*, 1977, **45**, 3–11.
- 6 At high Reynolds numbers it is possible to generate thrust by moving a stiff oar up and down at different speeds. The momentum of the water is different when being moved fast (down-beat of the oar) or slowly (up-beat of the oar). This is the principle how a scallop is able to move in water. However, at the low Reynolds number, the up and down movements of a stiff oar do not yield a net propulsion but simply a back and forth movement because the flow is reversible. This is referred to as the scallop theorem in Purcell's paper "Life at Low Reynolds Number".
- 7 M. Werner and L. W. Simmons, *Biol. Rev.*, 2008, **83**, 191–208.
- 8 H. C. Berg and R. A. Anderson, *Nature*, 1973, **245**, 380–382.
- 9 D. Bray, *Cell Movements*, Garland Pub., New York, 2001.
- 10 H. C. Berg, *E. coli in Motion*, Springer-Verlag, New York, 2004.
- 11 L. Turner, W. S. Ryu and H. C. Berg, *J. Bacteriol.*, 2000, **182**, 2793–2801.
- 12 E. W. H. Jager, O. Inganas and I. Lundstrom, *Science*, 2000, **288**, 2335–2338.
- 13 G. A. Ozin, I. Manners, S. Fournier-Bidoz and A. Arsenault, *Adv. Mater.*, 2005, **17**, 3011–3018.
- 14 J. J. Abbott, Z. Nagy, F. Beyeler and B. J. Nelson, *IEEE Robotics & Automation Magazine*, 2007, **14**, 92–103.
- 15 J. J. Abbott, K. E. Peyer, M. Cosentino Lagomarsino, L. Zhang, L. X. Dong, I. K. Kaliakatsos and B. J. Nelson, *Int. J. Rob. Res.*, 2009, **28**, 1434–1447.
- 16 V. Vogel and H. Hess, *Lect. Notes Phys.*, 2007, **711**, 367–383.
- 17 M. Burghard, *Angew. Chem., Int. Ed.*, 2008, **47**, 8565–8566.
- 18 M. Sitti, *Nature*, 2009, **458**, 1121–1122.
- 19 J. Clemmens, H. Hess, R. Doot, C. M. Matzke, G. D. Bachand and V. Vogel, *Lab Chip*, 2004, **4**, 83–86.
- 20 G. D. Bachand, H. Hess, B. Ratna, P. Satir and V. Vogel, *Lab Chip*, 2009, **9**, 1661–1666.
- 21 S. J. Ebbens and J. R. Howse, *Soft Matter*, 2010, **6**, 726–738.
- 22 W. F. Paxton, K. C. Kistler, C. C. Olmeda, A. Sen, S. K. St Angelo, Y. Y. Cao, T. E. Mallouk, P. E. Lammert and V. H. Crespi, *J. Am. Chem. Soc.*, 2004, **126**, 13424–13431.
- 23 T. R. Kline, W. F. Paxton, T. E. Mallouk and A. Sen, *Angew. Chem., Int. Ed.*, 2005, **44**, 744–746.
- 24 J. Burdick, R. Laocharoensuk, P. M. Wheat, J. D. Posner and J. Wang, *J. Am. Chem. Soc.*, 2008, **130**, 8164–8165.
- 25 R. Laocharoensuk, J. Burdick and J. Wang, *ACS Nano*, 2008, **2**, 1069–1075.
- 26 S. Sundararajan, P. E. Lammert, A. W. Zudans, V. H. Crespi and A. Sen, *Nano Lett.*, 2008, **8**, 1271–1276.
- 27 R. F. Ismagilov, A. Schwartz, N. Bowden and G. M. Whitesides, *Angew. Chem., Int. Ed.*, 2002, **41**, 652–654.
- 28 S. Fournier-Bidoz, A. C. Arsenault, I. Manners and G. A. Ozin, *Chem. Commun.*, 2005, 441–443.
- 29 T. R. Kline, J. Iwata, P. E. Lammert, T. E. Mallouk, A. Sen and D. Velegol, *J. Phys. Chem. B*, 2006, **110**, 24513–24521.
- 30 J. R. Howse, R. A. L. Jones, A. J. Ryan, T. Gough, R. Vafabakhsh and R. Golestanian, *Phys. Rev. Lett.*, 2007, **99**, 048102.
- 31 A. A. Solovev, Y. F. Mei, E. B. Urena, G. S. Huang and O. G. Schmidt, *Small*, 2009, **5**, 1688–1692.
- 32 W. F. Paxton, S. Sundararajan, T. E. Mallouk and A. Sen, *Angew. Chem., Int. Ed.*, 2006, **45**, 5420–5429.
- 33 T. E. Mallouk and A. Sen, *Sci. Am.*, 2009, **300**, 72–77.
- 34 J. Wang, *ACS Nano*, 2009, **3**, 4–9.
- 35 T. Mirkovic, N. S. Zacharia, G. D. Scholes and G. A. Ozin, *Small*, 2010, **6**, 159–167.
- 36 J. Wang and K. M. Manesh, *Small*, 2010, **6**, 338–345.
- 37 T. Mirkovic, N. S. Zacharia, G. D. Scholes and G. A. Ozin, *ACS Nano*, 2010, **4**, 1782–1789.
- 38 M. Hildebrand, *J. Mammal.*, 1959, **40**, 481–495.
- 39 T. Honda, K. I. Arai and K. Ishiyama, *IEEE Trans. Magn.*, 1996, **32**, 5085–5087.
- 40 K. Ishiyama, K. I. Arai, M. Sendoh and A. Yamazaki, *Proceedings of the 2000 International Symposium on Micromechanics and Human Science*, Nagoya, Japan, 2000.
- 41 K. Ishiyama, M. Sendoh, A. Yamazaki and K. I. Arai, *Sens. Actuators, A*, 2001, **91**, 141–144.
- 42 M. Sendoh, K. Ishiyama, K. I. Arai, M. Jojo, F. Sato and H. Matsuki, *IEEE Trans. Magn.*, 2002, **38**, 3359–3361.
- 43 M. Sendoh, K. Ishiyama and K. I. Arai, *IEEE Trans. Magn.*, 2003, **39**, 3232–3234.
- 44 M. Sendoh, A. Yamazaki, A. Chiba, M. Soma, K. Ishiyama and K. I. Arai, *Proceedings of the 2004 International Symposium on Micro-Nanomechanics and Human Science*, Nagoya, Japan, 2004.
- 45 R. Dreyfus, J. Baudry, M. L. Roper, M. Fermigier, H. A. Stone and J. Bibette, *Nature*, 2005, **437**, 862–865.
- 46 L. Zhang, E. Deckhardt, A. Weber, C. Schonenberger and D. Grutzmacher, *Nanotechnology*, 2005, **16**, 655–663.
- 47 D. J. Bell, L. X. Dong, B. J. Nelson, M. Golling, L. Zhang and D. Grutzmacher, *Nano Lett.*, 2006, **6**, 725–729.
- 48 L. Zhang, E. Ruh, D. Grutzmacher, L. X. Dong, D. J. Bell, B. J. Nelson and C. Schonenberger, *Nano Lett.*, 2006, **6**, 1311–1317.
- 49 D. J. Bell, S. Leutenegger, K. M. Hammar, L. X. Dong and B. J. Nelson, *Proceedings of the 2007 IEEE International Conference on Robotics and Automation*, Rome, Italy, 2007.
- 50 L. Zhang, J. J. Abbott, L. X. Dong, B. E. Kratochvil, D. Bell and B. J. Nelson, *Appl. Phys. Lett.*, 2009, **94**, 064107.
- 51 A. Ghosh and P. Fischer, *Nano Lett.*, 2009, **9**, 2243–2245.
- 52 H. C. Berg and D. A. Brown, *Nature*, 1972, **239**, 500–504.
- 53 L. Zhang, J. J. Abbott, L. X. Dong, K. E. Peyer, B. E. Kratochvil, H. X. Zhang, C. Bergeles and B. J. Nelson, *Nano Lett.*, 2009, **9**, 3663–3667.
- 54 N. Darnton, L. Turner, K. Breuer and H. C. Berg, *Biophys. J.*, 2004, **86**, 1863–1870.
- 55 D. B. Weibel, P. Garstecki, D. Ryan, W. R. Diluzio, M. Mayer, J. E. Seto and G. M. Whitesides, *Proc. Natl. Acad. Sci. U. S. A.*, 2005, **102**, 11963–11967.
- 56 S. Martel, C. C. Tremblay, S. Ngakeng and G. Langlois, *Appl. Phys. Lett.*, 2006, **89**, 233904.
- 57 E. Steager, C. B. Kim, J. Patel, S. Bith, C. Naik, L. Reber and M. J. Kim, *Appl. Phys. Lett.*, 2007, **90**, 263901.
- 58 B. Behkam and M. Sitti, *Appl. Phys. Lett.*, 2008, **93**, 223901.
- 59 B. A. Korgel, *Science*, 2005, **309**, 1683–1684.
- 60 S. Amelinckx, X. B. Zhang, D. Bernaerts, X. F. Zhang, V. Ivanov and J. B. Nagy, *Science*, 1994, **265**, 635–639.
- 61 E. D. Sone, E. R. Zubarev and S. I. Stupp, *Angew. Chem., Int. Ed.*, 2002, **41**, 1706–1709.
- 62 P. X. Gao, Y. Ding, W. J. Mai, W. L. Hughes, C. S. Lao and Z. L. Wang, *Science*, 2005, **309**, 1700–1704.
- 63 M. Nath and B. A. Parkinson, *J. Am. Chem. Soc.*, 2007, **129**, 11302–11303.
- 64 C. B. Cao, H. L. Du, Y. J. Xu, H. S. Zhu, T. H. Zhang and R. Yang, *Adv. Mater.*, 2008, **20**, 1738–1743.
- 65 J. Yu, Y. J. Qiu, X. X. Zha, M. Yu, J. L. Yu, J. Rafique and J. Yin, *Eur. Polym. J.*, 2008, **44**, 2838–2844.
- 66 N. Anscombe, *Nat. Photonics*, 2010, **4**, 22–23.

- 67 V. Y. Prinz, V. A. Seleznev, A. K. Gutakovskiy, A. V. Chehovskiy, V. V. Preobrazhenskii, M. A. Putyato and T. A. Gavrilova, *Physica E (Amsterdam)*, 2000, **6**, 828–831.
- 68 O. G. Schmidt and K. Eberl, *Nature*, 2001, **410**, 168–168.
- 69 L. Zhang, S. V. Golod, E. Deckardt, V. Prinz and D. Grutzmacher, *Physica E (Amsterdam)*, 2004, **23**, 280–284.
- 70 A. Cho, *Science*, 2006, **313**, 164–165.
- 71 L. Zhang, L. X. Dong, D. J. Bell, B. J. Nelson, C. Schoenenberger and D. Grutzmacher, *Microelectron. Eng.*, 2006, **83**, 1237–1240.
- 72 L. Zhang, L. X. Dong and B. J. Nelson, *Appl. Phys. Lett.*, 2008, **92**, 143110.
- 73 O. G. Schmidt, N. Schmarje, C. Deneke, C. Muller and N. Y. Jin-Phillipp, *Adv. Mater.*, 2001, **13**, 756–759.
- 74 Y. F. Mei, G. S. Huang, A. A. Solovov, E. B. Urena, I. Moench, F. Ding, T. Reindl, R. K. Y. Fu, P. K. Chu and O. G. Schmidt, *Adv. Mater.*, 2008, **20**, 4085–4090.
- 75 V. Luchnikov, O. Sydorenko and M. Stamm, *Adv. Mater.*, 2005, **17**, 1177–1182.
- 76 P. Tyagi, N. Bassik, T. G. Leong, J. H. Cho, B. R. Benson and D. H. Gracias, *J. Microelectromech. Syst.*, 2009, **18**, 784–791.
- 77 M. J. Brett and M. M. Hawkeye, *Science*, 2008, **319**, 1192–1193.
- 78 F. B. Hagedorn and E. M. Gyorgy, *J. Appl. Phys.*, 1968, **39**, 995–997.
- 79 K. Ishiyama, K. I. Arai, M. Sendoh and A. Yamazaki, *Journal of Micromechatronics*, 2003, **2**, 77–86.
- 80 N. C. Darnton, L. Turner, S. Rojevsky and H. C. Berg, *J. Bacteriol.*, 2007, **189**, 1756–1764.
- 81 E. Lauga, W. R. DiLuzio, G. M. Whitesides and H. A. Stone, *Biophys. J.*, 2006, **90**, 400–412.
- 82 K. E. Peyer, L. Zhang, B. E. Kratochvil and B. J. Nelson, *Proceedings of the 2010 IEEE International Conference on Robotics and Automation Anchorage*, Alaska, USA, 2010.
- 83 E. M. Purcell, *Proc. Natl. Acad. Sci. U. S. A.*, 1997, **94**, 11307–11311.
- 84 S. Chattopadhyay, R. Moldovan, C. Yeung and X. L. Wu, *Proc. Natl. Acad. Sci. U. S. A.*, 2006, **103**, 13712–13717.
- 85 K. E. Peyer, L. Zhang, B. E. Kratochvil and B. J. Nelson, unpublished work.
- 86 G. J. Hancock, *Proc. R. Soc. London, Ser. A*, 1953, **217**, 96–121.
- 87 J. Gray, *J. Exp. Biol.*, 1955, **32**, 802–814.
- 88 R. G. Cox, *J. Fluid Mech.*, 1970, **44**, 791–810.
- 89 J. Lighthill, *SIAM Rev.*, 1976, **18**, 161–230.
- 90 G. Taylor, *Proc. R. Soc. London, Ser. A*, 1951, **209**, 447–461.
- 91 K. E. Peyer, *Master thesis*, ETH Zurich, 2009.
- 92 J. Lighthill, *Mathematical Biofluidynamics*, SIAM, Philadelphia, PA, 1975.
- 93 O. Pironneau and D. F. Katz, in *Optimal swimming of Motion of Flagella Swimming and Flying in Nature*, ed. T. Y. Wu, Plenum, New York, 1975, vol. 1.
- 94 J. J. L. Higdon, *J. Fluid Mech.*, 1979, **94**, 331–351.
- 95 J. J. L. Higdon, *J. Fluid Mech.*, 1979, **90**, 685–711.
- 96 T. Fujita and T. Kawai, *JSME Int. J., Ser. C*, 2001, **44**, 952–957.
- 97 L. Zhang, J. J. Abbott, L. X. Dong, B. E. Kratochvil, H. X. Zhang, K. E. Peyer and B. J. Nelson, *Proceedings of IEEE/RSJ 2009 International Conference on Intelligent Robots and Systems (IROS2009)*, St Louis, MO, USA, 2009.
- 98 J. S. Randhawa, T. G. Leong, N. Bassik, B. R. Benson, M. T. Jochmans and D. H. Gracias, *J. Am. Chem. Soc.*, 2008, **130**, 17238–17239.
- 99 R. Fernandes and D. H. Gracias, *Mater. Today*, 2009, **12**, 14–20.
- 100 T. G. Leong, C. L. Randall, B. R. Benson, N. Bassik, G. M. Stern and D. H. Gracias, *Proc. Natl. Acad. Sci. U. S. A.*, 2009, **106**, 703–708.
- 101 T. G. Leong, C. L. Randall, B. R. Benson, A. M. Zarafshar and D. H. Gracias, *Lab Chip*, 2008, **8**, 1621–1624.
- 102 D. Weihs, T. G. Mason and M. A. Teitell, *Biophys. J.*, 2006, **91**, 4296–4305.
- 103 D. Sanchez, N. Johnson, C. Li, P. Novak, J. Rheinlaender, Y. J. Zhang, U. Anand, P. Anand, J. Gorelik, G. I. Frolenkov, C. Benham, M. Lab, V. P. Ostannin, T. E. Schaffer, D. Klenerman and Y. E. Korchev, *Biophys. J.*, 2008, **95**, 3017–3027.
- 104 K. Yum, N. Wang and M. F. Yu, *Nanoscale*, 2010, **2**, 363–372.
- 105 F. Obataya, C. Nakamura, S. W. Han, N. Nakamura and J. Miyake, *Biosens. Bioelectron.*, 2005, **20**, 1652–1655.
- 106 I. Obataya, C. Nakamura, S. Han, N. Nakamura and J. Miyake, *Nano Lett.*, 2005, **5**, 27–30.
- 107 D. Cai, J. M. Mataraza, Z. H. Qin, Z. P. Huang, J. Y. Huang, T. C. Chiles, D. Carnahan, K. Kempa and Z. F. Ren, *Nat. Methods*, 2005, **2**, 449–454.
- 108 W. Kim, J. K. Ng, M. E. Kunitake, B. R. Conklin and P. D. Yang, *J. Am. Chem. Soc.*, 2007, **129**, 7228–7229.
- 109 T. W. R. Fountain, P. V. Kailat and J. J. Abbott, *Proceedings of the 2010 IEEE International Conference on Robotics and Automation*, Anchorage, Alaska, USA, 2010.
- 110 S. Pennathur, *Lab Chip*, 2008, **8**, 383–387.
- 111 A. Ashkin and J. M. Dziedzic, *Science*, 1987, **235**, 1517–1520.
- 112 P. Garstecki, P. Tierno, D. B. Weibel, F. Sagues and G. M. Whitesides, *J. Phys.: Condens. Matter*, 2009, **21**, 204110.
- 113 A. Teleki, M. Suter, P. R. Kidambi, O. Ergeneman, F. Krumeich, B. J. Nelson and S. E. Pratsinis, *Chem. Mater.*, 2009, **21**, 2094–2100.
- 114 W. S. Seo, J. H. Lee, X. M. Sun, Y. Suzuki, D. Mann, Z. Liu, M. Terashima, P. C. Yang, M. V. McConnell, D. G. Nishimura and H. J. Dai, *Nat. Mater.*, 2006, **5**, 971–976.